# Understanding the mechanism of facilitation in hoverfly TSDNs

Anindya Ghosh[1*], Sarah Nicholas[2], Karin Nordström[2], Thomas Nowotny[1], James Knight[1]

**1** Sussex AI, School of Engineering and Informatics, University of Sussex, Brighton, UK

**2** Flinders Health and Medical Research Institute, Flinders University, Adelaide, South Australia, Australia

* anindya128@yahoo.com

## Abstract

Many animals use visual motion cues to track and pursue small, fast-moving targets, for instance, prey or conspecifics. In target-pursuing insects, including dragonflies and hoverflies, Small Target Motion Detector (STMD) neurons are found in the optic lobes and are believed to be presynaptic to Target Selective Descending Neurons (TSDNs) that project to motor command centres. While STMDs respond robustly to target motion – even when displayed against moving backgrounds – TSDN target responses are modulated by background motion. Depending on whether the background motion is syn- or contra-directional to the target motion, the response of the TSDNs is either suppressed or facilitated (amplified). This suggests additional input from neurons tuned to background motion. However, the neural mechanism is not clearly understood. To explore the underlying circuitry, we developed three candidate models of the TSDN circuit – which combine input from STMDs and optic flow-sensitive Lobula Plate Tangential Cells (LPTCs) in different ways – and fitted them to published electrophysiology data from hoverfly TSDNs. We then tested the best-fitting models against new electrophysiological data using different background patterns. We found that the overall best model suggests simple inhibition from LPTCs with the same preferred direction as the STMDs feeding into the TSDN. This parsimonious mechanism can explain the facilitation and suppression of TSDN responses to small targets and may inform similar studies in other animals and open new avenues for bio-inspired robotics.

## Introduction

In many species, the ability to detect small, moving targets in visual clutter is crucial for survival. For example, for a predator, these targets may represent prey, while in other animals, they may represent rivals or potential mates [1]. Thus, neural circuits underlying target-detection have been heavily studied and target-detection behaviours have been described in a range of species, including salamanders [2], zebrafish larvae [3], dragonflies [4], and hoverflies [5].

In insects, target-detection behaviours are believed to be driven by target-tuned neurons found throughout the visual and pre-motor regions [6]. Specifically, in hoverflies, two types of target-tuned neurons can be found – the Small Target Motion Detectors (STMDs) in the optic lobe [7, 8], and the Target Selective Descending

Neurons (TSDNs) [9] that connect the central brain with motor command centres in the thoracic ganglia. Surprisingly, STMDs are able to respond robustly to small, moving targets in visually cluttered environments, even when there is no relative motion between the target and the background [10]. In contrast, the responses of their post-synaptic targets, the TSDNs, are modulated by background motion [11]. Depending on whether the background motion is syn- or contra-directional to the target motion, the TSDN response can be either suppressed or facilitated compared to the response to a target against a stationary background.

There are many models for the detection of motion, such as the classic Elementary Motion Detectors (EMDs), which perform a non-linear comparison of signals from two points in space after delaying one of them [12–15]. This leads to a directional response to motion. While there is compelling evidence that Lobula Plate Tangential Cells (LPTCs) – optic lobe neurons that respond to widefield motion – are driven by spatially pooled EMDs, LPTCs are not target-tuned. Therefore, other models have been developed to explain the mechanisms behind the detection of targets amidst clutter. These generally act as matched filters [16, 17] or use a centre-surround mechanism [18]. The matched filter model, often referred to as a 1-point correlator or an Elementary STMD (ESTMD), is based on the comparison of ON (brightness increment) and OFF (brightness decrement) signals from one point in space. The ESTMD takes advantage of the unique temporal signature associated with a dark target – where a leading OFF edge is immediately followed by a trailing ON edge – and responds only to small, dark, moving objects, while being generally unaffected by background motion. A consequence of 1-point correlator models is that, if similar target-like spatio-temporal signatures are found in the background, they will also elicit a response, which is indeed seen in dragonfly STMDs [17]. Furthermore, both STMDs and TSDNs respond poorly to signals containing only leading OFF or trailing ON edges [11, 17], suggesting that similar circuitry underlies both types of neurons.

However, existing models of small-object detection [16, 18, 19] fail to explain why hoverfly TSDNs *are* affected by background motion. Therefore, additional mechanisms are needed and we hypothesised that both target-specific and optic-flow sensitive neurons are necessary to mechanistically describe the TSDN circuit. To test this, we made the output of the Elementary STMD (ESTMD) model [16] directionally-selective, tiled them over the visual field and spatially pooled their outputs to match biological STMD [20] and TSDN receptive fields [11]. We modelled optic-flow sensitive LPTCs using EMDs (Hassenstein-Reichardt detectors) [13] and then fitted plausible TSDN circuit arrangements, combining the STMD and LPTC outputs, to already published electrophysiological data from TSDNs [11]. Subsequently, we acquired new biological data where TSDNs responded to targets against different backgrounds and tested the candidate circuits on this new data to assess whether the models generalise. This led us to discard one of the circuits. To determine the most viable of the remaining two candidate circuits, we then tested them on the stimuli described in [11], allowing us to eliminate all but one circuit. Finally, we discuss how this circuit can mechanistically explain observations from biological TSDNs. Thus, by combining existing neuron models of STMDs and LPTCs, we obtain circuit configurations that can, for the first time, plausibly explain the phenomenon of facilitation and suppression observed in biological TSDNs [11].

# Results

To model the responses of hoverfly TSDNs to targets moving against background motion, we took advantage of existing ESTMD [16, 21] and EMD models [12, 14]. To facilitate the continuity of the ESTMD model literature, the naming conventions of the

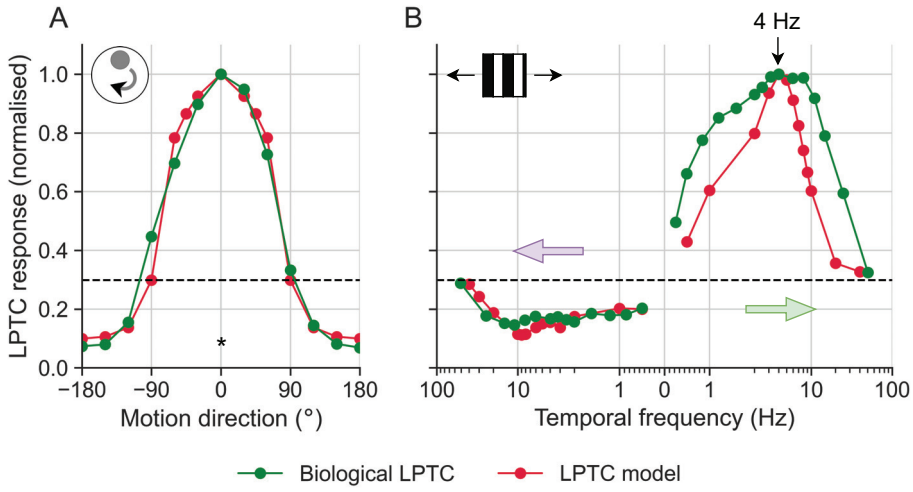


**Fig 1. Velocity tuning of model and biological LPTCs.** (**A**) Local motion direction tuning curve obtained using a dot stimulus (see ref [22] for stimulus details). The asterisk (*) denotes the preferred. (**B**) Temporal frequency tuning to an 11.4° wavelength, square-wave vertical grating stimulus, with Michelson contrast of 95%. The green and purple arrows indicate motion in the preferred direction (PD) and null direction (ND), respectively. In both panels, the dashed black line denotes the spontaneous activity, and the model data represents the mean normalised response over 0.5 s stimulation. The biological LPTC data was obtained from ref [22].

mechanisms described here are equivalent to those used elsewhere [16, 21].

### LPTC model captures direction and velocity tuning of biological LPTCs

The LPTC was modelled by spatially pooling output from local elementary motion detectors (EMDs) (see Lobula Plate Tangential Cell (LPTC) modelling section). Biological data from a blowfly H2 neuron – an LPTC in the fly lobula – was used to compare the model LPTC tuning with biology (Fig 1). Using a 20° diameter dot stimulus, Longden et al. [22] obtained the local motion direction tuning of the H2 neuron at 0° elevation and 30° azimuth. We used a similar dot stimulus to obtain local motion direction tuning for our model LPTC (red data, Fig 1A), with a preferred direction to the right (0°) and an asymmetry to preferred and anti-preferred direction motion about the spontaneous activity rate.

Fig 1B shows that the model also closely matches the temporal frequency tuning of the biological LPTC in both the preferred (green arrow) and anti-preferred direction (purple arrow). This was tested using a vertical square-wave grating with a wavelength of 11.4° and Michelson contrast of 95%, presented for 0.5 ms. In both biology and the model, the maximal response occurs around 4 Hz.

Longden et al. [22] found that biological LPTCs start responding to square-wave grating stimuli 20−60 ms after stimulus onset (green data, Fig 2A). In response to a 4 Hz stimulus, our model captures the response onset dynamics of biological LPTCs well (Fig 2A). We quantified the mean response within a 20−60 ms time window across temporal frequencies and found that our model LPTC mimicked biological data well (Fig 2B). Compared to the tuning curves in Fig 1B, those in Fig 2B peak at a higher temporal frequency. This can be attributed to the fact that the response onset decreases

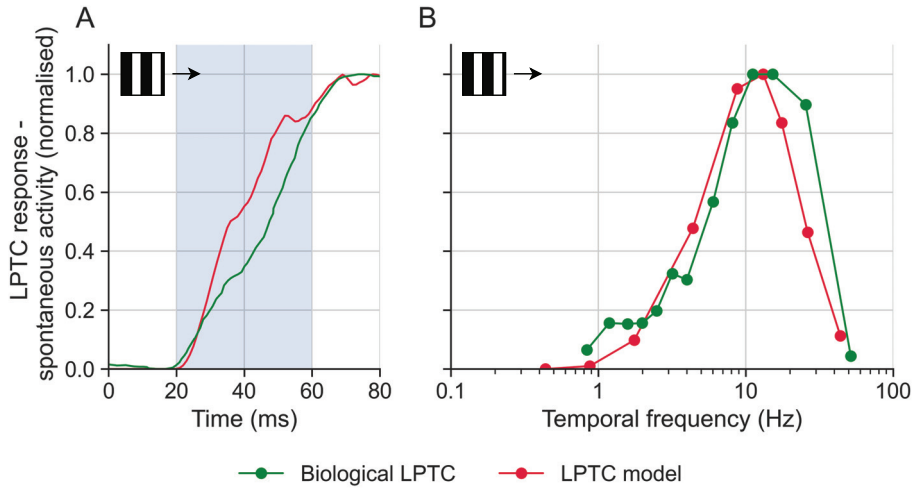


**Fig 2. Transient LPTC response characteristics of model and biological LPTCs.** (**A**) The response onset to a 4 Hz stimulus, smoothed with a Gaussian filter with $\sigma = 6$ ms. The stimulus appeared and started moving at 0 ms. The shaded region shows the analysis window used in panel B. (**B**) The transient response (averaged over the 20−60 ms period shown in panel (A) to preferred direction motion as a function of temporal frequency. The spontaneous activity has been subtracted. The biological LPTC data was obtained from ref [22]. All responses are normalised to their peak.

with temporal frequency [23]. In summary, our LPTC model responses closely match those of their biological counterparts (Fig 1 and Fig 2).

### The dynamics of our STMD model matches hoverfly biology

Hoverfly STMDs vary in their directional selectivity as well as receptive field size and location [10]. However, in this work, we focus on a subset of STMDs known as small-field STMDs [20], which have small, fronto-dorsal receptive fields and can be directionally selective. Barnett et al. [20] determined size selectivity using a black bar with a fixed width (parallel to the direction of target motion) and varying height (perpendicular to the direction of target motion) moving at a constant speed. They found that male *Eristalis tenax* small-field STMDs give peak responses to targets with a height of 1.6° (see [20]; green data, Fig 3A).

In hoverflies, the velocity response function has only been published for STMDs in females (see [7]; green data, Fig 3B). This was determined using a black square of fixed size moving at a range of speeds in the neuron's preferred direction. The resulting velocity response function shows a peak response around 30−200°/s [7]. Wiederman et al. [16] and Bagheri et al. [21] proposed an elementary STMD (ESTMD) model that encapsulates this behaviour, which we reproduced (see Methods for algorithmic details of the STMD model). In this model, each delayed OFF (brightness decrement) signal is correlated with an undelayed ON (brightness increment) signal from the same point in space, thus acting as a detector for a dark target moving on a brighter background. We modified the temporal adaptation time constants (see Supplementary section), which resulted in a narrower velocity tuning (red data, Fig 3B). Nevertheless, our STMD model closely matches Wiederman et al.'s [16] ESTMD model (Fig 3). While there are differences between biology and the models (Fig 3), these are

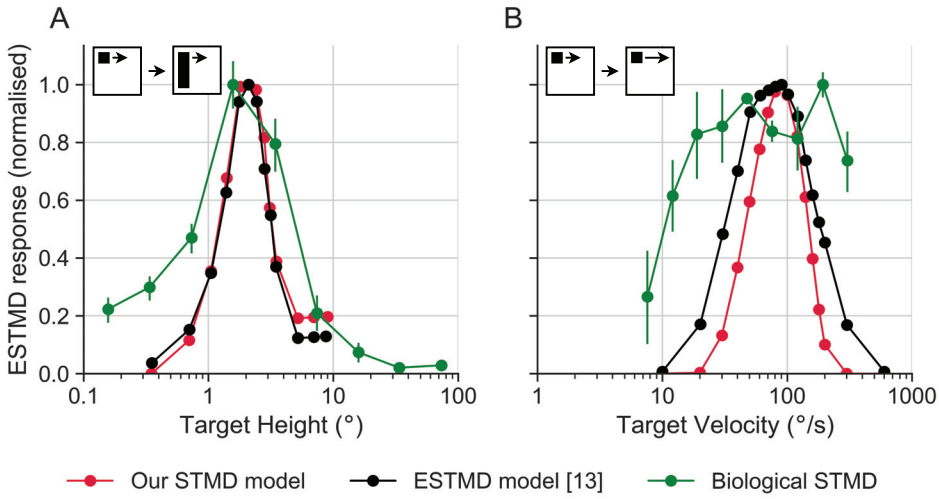


**Fig 3. Comparison of spatiotemporal characteristics from model and biological STMDs.** (**A**) Normalised responses to targets of different heights. The bar had a constant width of 0.8° and was moving at 50°/s. In modelling, we used bar heights between 0.35° and 9°. The biological STMD data is from ref [20](**B**) Velocity tuning of black, square targets (0.8°×0.8°). In modelling, we used velocities in the 10−600°/s range. The biological STMD data is from [10].

outside the range of target speeds and sizes used in the rest of the paper.

As TSDNs are directionally selective [1], they likely receive input from directionally selective STMDs. To capture this in our modelling, we passed the ESTMD model output through an EMD, resulting in directional selectivity. In addition, we spatially pooled output from the directionally selective ESTMDs to match the receptive fields of small-field STMDs [1, 20]. Details about the directionally-selective STMD model are in the Methods.

### TSDN circuit arrangements

TSDNs are likely to be post-synaptic to STMDs [6]. In addition, as TSDN responses are affected by background motion, TSDNs are likely to receive additional input from LPTCs. As syn-directional background motion inhibits TSDN response to target motion [11, 24], it seems plausible that they receive inhibitory input from LPTCs with the same preferred direction. In addition, TSDNs are facilitated by contra-directional background motion [11], suggesting that they receive input from neurons with the opposite preferred direction. As the background used in the facilitation experiments consisted of a starfield pattern with many target-sized features, the facilitation could come from additional LPTCs or STMDs. However, additive inputs from these can be discarded categorically for the following reasons:

1. LPTCs cannot directly excite the TSDN as this would result in TSDN responses to wide-field optic flow even in the absence of a target. This does not occur in biological TSDNs [11, 24].

2. The input from an STMD with the opposite preferred direction cannot directly excite the TSDN, as this would result in TSDN responses to both directions of

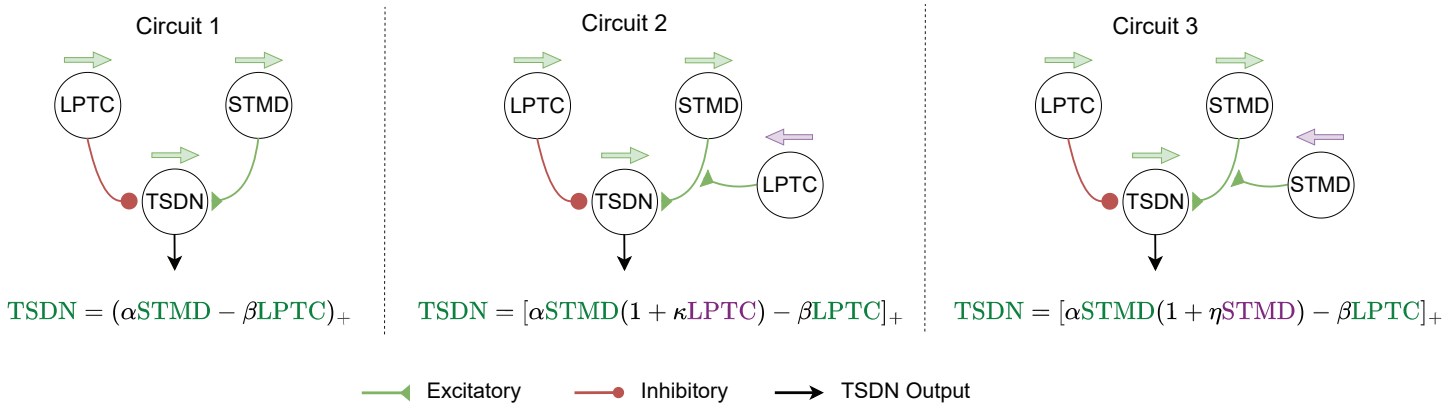


**Fig 4. Candidate Model Circuits**. All circuits include direct excitatory input from STMDs. *Left*. Circuit 1 involves a simple linear subtraction of the LPTC response from the STMD response. All neurons in the circuit have the same preferred direction (green arrows). *Middle*. Circuit 2 additionally includes an LPTC with the opposite preferred direction (purple arrow) multiplicatively amplifying the STMD signal. *Right*. Circuit 3 involves the addition of an STMD with the opposite preferred direction (purple arrow) multiplicatively amplifying the signal from the STMD. The circuits are reflected in the functional equations below each. $\alpha$, $\beta$, $\kappa$ and $\eta$ are the coefficients of the relevant terms.

motion, which does not occur in biological TSDNs - they are directionally selective [1].

Thus, we evaluate three plausible circuit arrangements. Circuit 1 involves a linear summation of STMD and LPTC inputs (*left*, Fig 4). This has an obvious implication – if a hoverfly is stationary or *hovering*, due to a lack of self-generated optic flow there would be no input from the LPTC, and therefore the TSDN output would be identical to the output of a TSDN receiving only STMD input.

Circuit 2 is an extension of circuit 1, with additional excitatory input from an LPTC with the opposite preferred direction. This LPTC (purple arrow, *middle*, Fig 4), enhances any STMD signals, but does nothing if the STMD is inactive. Thus, in many cases, the outputs of circuits 1 and 2 are the same. However, in the event of background motion contra-directional to target motion, the STMD signal would receive an additional *boost* in circuit 2, thus resulting in a facilitated TSDN response.

Circuit 3 also amplifies the STMD input to the TSDN (purple arrow, *right*, Fig 4). However, in circuit 3, the amplification comes from an STMD with the opposite preferred direction of motion. For facilitation, circuit 3 thus relies on the background consisting of target-like objects, such as the 'starfield' background used in the published recordings of biological TSDNs [11].

### Comparisons of candidate TSDN circuits

We fit the three neuronal weight coefficients ($\alpha$, $\beta$, $\kappa$ and $\eta$ where relevant) and the LPTC equation (Lobula Plate Tangential Cell (LPTC) modelling section) coefficients ($g$, $\gamma$ and $s$) of our three candidate TSDN circuits to minimise the mean root-mean-square error (RMSE) against published TSDN recordings of targets moving on a starfield background [11]. In these experiments, the background consisted of thousands of targets moving horizontally to mimic the perspective-corrected optic flow generated by the viewer sideslipping at 50 cm/s [25]. In circuit 2, where two LPTCs are present, we only

**Table 1.** Neuronal weight and LPTC equation coefficients.

| **Circuit** | **LPTC equation** | | | **Neuronal weight** | | | |
|---|---|---|---|---|---|---|---|
| | $g$ | $\gamma$ | $s$ | $\alpha$ | $\beta$ | $\kappa$ | $\eta$ |
| STMD only | - | - | - | 0.4 | - | - | - |
| Circuit 1 | 13 | 0.3 | 10 | 0.8 | 13.9 | - | - |
| Circuit 2 | 11 | 0.9 | 10 | 0.3 | 29.9 | 2 | - |
| Circuit 3 | 13 | 0.3 | 10 | 0.5 | 4.7 | - | 1 |

optimised a single set of LPTC coefficients. We use an 'STMD only' circuit as a benchmark to normalise the circuit errors. This circuit comprises an STMD output weighted by the STMD neuronal coefficient $\alpha$. The coefficients obtained are shown in Table 1.

Fig 5 shows the model and biological responses of a single TSDN to a target moving over either a bright background ('alone', Fig 5) or over a starfield background (data replotted from [11]). When the target moves across a bright screen or against a stationary pattern ('alone' and 'stationary', Fig 5), all the outputs are similar. However, when the target is displayed over a starfield background moving in the same direction as the target, all TSDN circuits are strongly inhibited ('syn', Fig 5). In contrast, the STMD output remains unchanged, as expected from previous work [10, 16, 21]. When the target is displayed over a starfield background moving in the opposite direction, all TSDN circuits are facilitated ('contra', Fig 5), whereas the STMD output remains largely unaffected, as expected [10, 16, 21]. However, note that the 'contra' response from circuit 2 seems to 'overshoot' the biological TSDN response.

Since LPTCs have a spontaneous rate, even in the 'alone' and 'stationary' conditions, when there is no background motion, circuits 1 and 2 receive non-zero input from the LPTCs, which results in a more involved navigation through the hyperparameter search space. However, for circuit 3, since in 'alone' and 'stationary' conditions, only the target moves and STMDs do not have a spontaneous rate, the output of the STMD with the opposite preferred direction (purple arrow, refer to Figure 4) is zero. This allows the synaptic weight of this amplifying STMD, $\eta$, to be tuned specifically towards minimising the fitting error for the 'contra'-directional condition. Indeed, for this example neuron (Fig 5), circuit 3 fits the biological TSDN data remarkably well.

To compare this across neurons [11] we calculated the mean Root-Mean-Square-Error (RMSE) for each circuit per condition (Fig 6) normalised against the equivalent RMSE of a TSDN circuit with only an STMD input ('STMD only'). For each neuron simulation, we used the same initial conditions, i.e. the same starting points for the target as was used in the electrophysiology experiments, and took each neuron's receptive field into account (see Methods for details). We found that 'syn' resulted in the smallest errors for all circuits, whereas 'contra' led to the largest errors. However, it should be noted that with syn-directional motion, TSDN responses tend to be suppressed to near-zero values (Fig 6; [11]). This is because the 'STMD only' circuit lacks an LPTC component and thus, inherently attempts to *average* across the hyperparameter search space. This can be seen in the 'syn' panel of Fig 5 where the 'STMD only' response shows no suppression.

Across background conditions, and across neurons, circuit 1 performs better than circuit 2, and circuit 3 outperforms both circuits 1 and 2 (Fig 6). All circuits outperform the 'STMD only' circuit – the normalised errors are all below 1. Thus, across neurons, the normalised mean RMSEs reflect the quality of the circuit fits exemplified for one neuron in Fig 5.

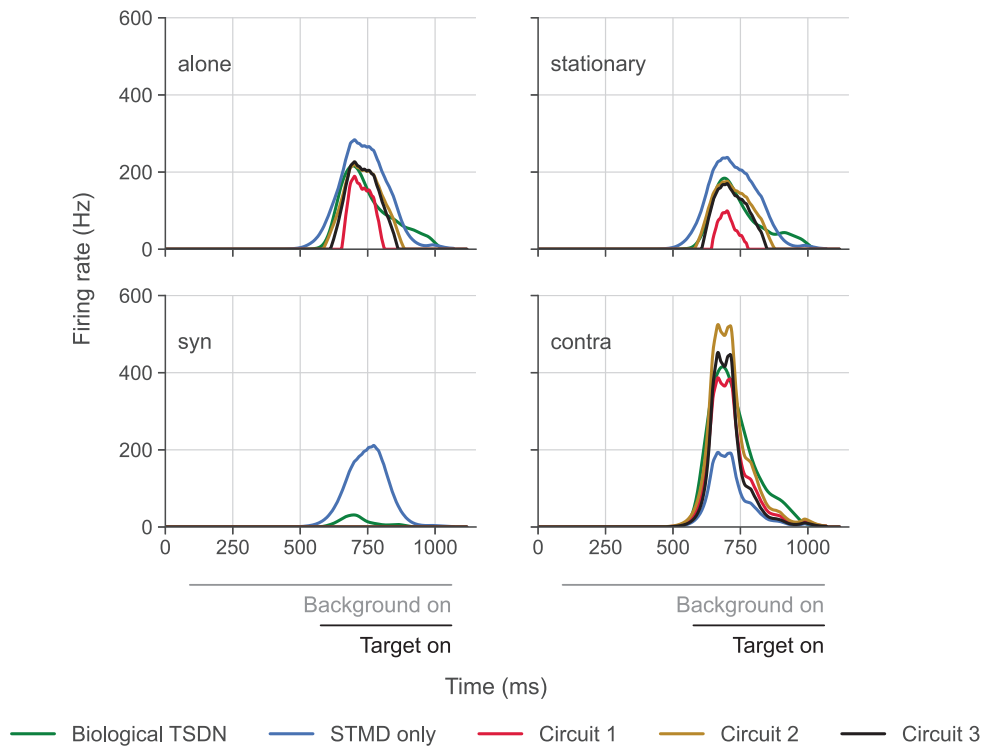


**Fig 5. Example TSDN model and biological outputs to targets moving over the starfield background.** The data show the spike histograms as a function of time from a single TSDN as it responds to a small target moving through its receptive field, in the neuron's preferred direction, at 900 pixels/s. The biological data is replotted from [11] (shown in green), and the outputs of the fitted circuits are in other colours. The different panels show the response to the black, circular target moving over a bright screen ('alone'), over a stationary starfield pattern ('stationary'), a sideslipping starfield (50 cm/s) in the same direction as the target ('syn'), or in the opposite direction ('contra'). The greyscale bars under the data indicate the peri-stimulus durations.

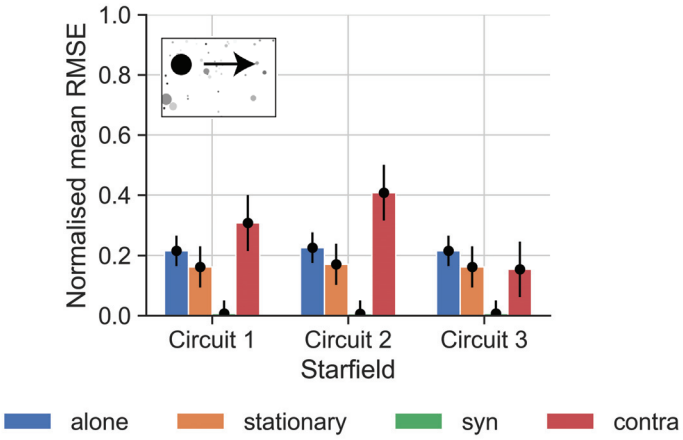


**Fig 6. Errors from fitting candidate circuits to biological TSDN data for targets moving over the starfield background.** For each neuron (N=35, data from [11]) we calculated the mean RMSE by comparing each circuit (described in Fig 4) with the electrophysiological data. The mean RMSE of each circuit per condition were then normalised by the equivalent RMSE of the 'STMD only' circuit. The whiskers of the black points (the mean RMSEs) indicate the variation across neurons, quantified as the standard deviation of the normalised mean RMSE of the particular bar plot.

### TSDN responses to targets moving across broadband backgrounds

When fitting the different circuits (Fig 6), we used published biological data where TSDNs responded to targets moving over a starfield background [11]. As the starfield background used in those experiments consists of thousands of target-like features, it could theoretically stimulate STMDs [16, 26] as well as LPTCs, making it difficult to separate the different circuits (Fig 4). We, therefore, generated new electrophysiological recordings against two other backgrounds – 'cloud' ($N = 10$) and 'sinusoidal' ($N = 6$), which are very unlikely to stimulate STMDs [10].

The cloud background has a 2D power spectrum similar to that of typical natural scenes and a mean luminance of $\approx 128$ where luminance $\in [0, 255]$ [24] with a Michelson contrast of 100% (see ref [7] for more details). As expected [24], TSDN responses to target motion are inhibited when the target is displayed against syn-directional 'cloud' background motion (Figs 7C, F, I). However, and more surprisingly considering earlier work [24], TSDN responses are strongly facilitated by contra-directional cloud background motion (Figs 7D, F, I).

The 'sinusoidal' background is a vertical sinusoidal grating with a wavelength of 7°, moving at 5 Hz, and a Michelson contrast of 25% which should not stimulate any STMDs [10]. Again, we found that TSDN responses were inhibited by syn-directional background motion, and facilitated by contra-directional background motion (Fig 7J).

While the new backgrounds allow us to test the robustness of all the fitted circuits, the viability of circuit 3, in particular, can be tested as it relies on STMD input for the facilitation, and thus on backgrounds that contain target-like features. Because, both the cloud and sinusoidal backgrounds are devoid of target-like features, the facilitation seen in the new electrophysiology (Fig 7) argues strongly against circuit 3.

Using the circuit coefficients listed in Table 1 – which we fitted on the starfield dataset – we tested each candidate circuit on the cloud and sinusoidal datasets (Fig 7). Similar to our initial testing on the starfield dataset, we used the same initial conditions,

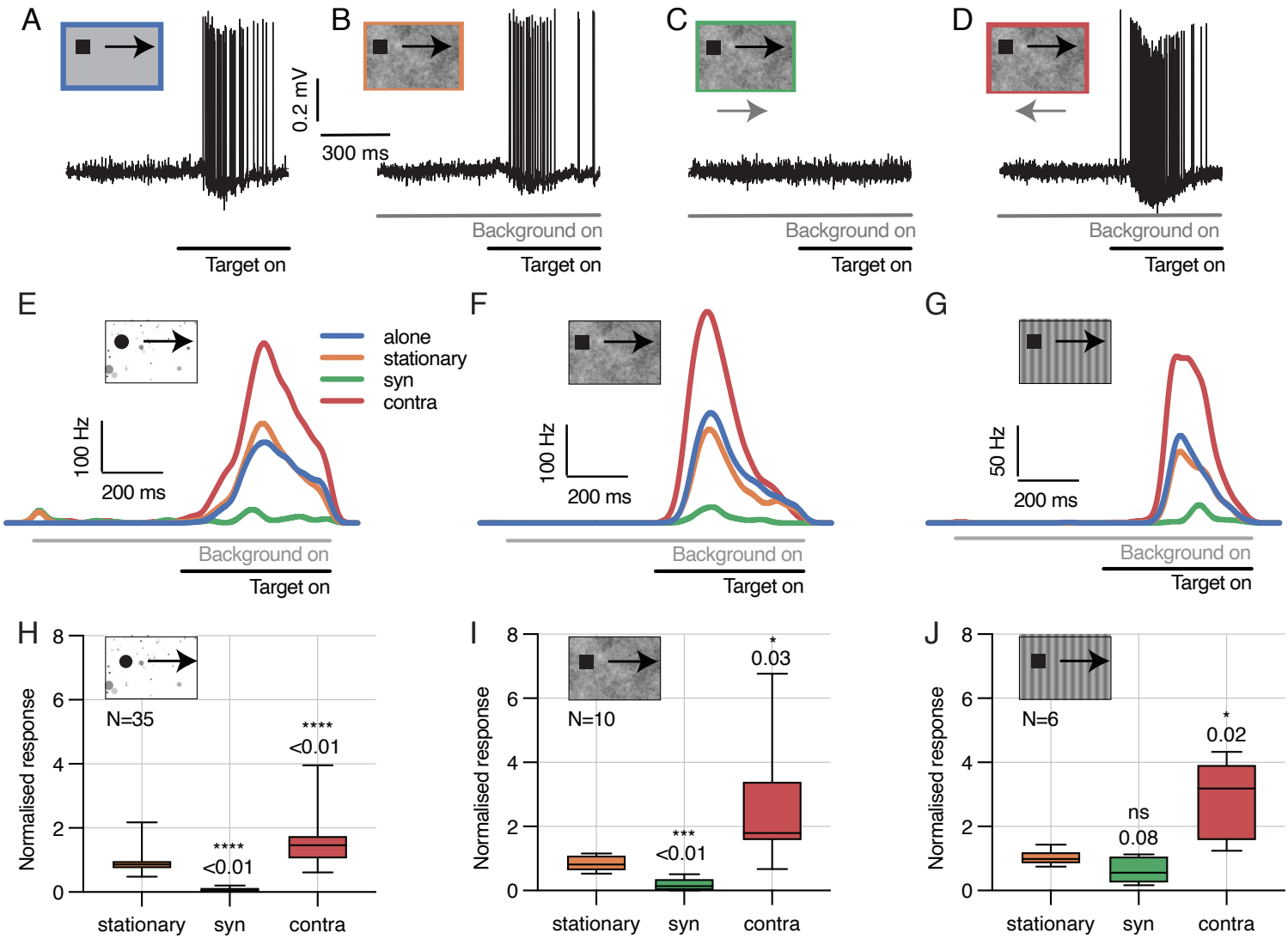


**Fig 7. New electrophysiological recordings of TSDNs responding to targets moving over cloud and sinusoidal backgrounds.** (**A-D**) Example raw electrophysiology data from a single TSDN responding to targets moving over a grey background ('alone'), or a 'stationary', 'syn'-directional or 'contra'-directional cloud background. The greyscale bars under the data show the stimulus timing. (**E-G**) Spike rate responses from three different TSDN neurons for four background conditions, using the starfield (E), cloud (F) or sinusoidal grating (G) background. In all cases, the data show the spike histograms averaged across repetitions (starfield: n=9 – 15 repetitions; cloud: n=24 repetitions; sinusoidal: n=30 repetitions), and converted to rates as described in Methods. (**H-J**) Boxplots of TSDN responses across neurons for starfield, cloud and sinusoidal backgrounds. The whiskers of the boxplots extend across the range of the data (min to max). In all cases, we calculated the average spike frequency across the entire time the target was on the screen and normalised this to the response to a target moving over a bright (panel H), or grey (panels I and J), background. The data in panel E, H is replotted from [11]. Stars indicate statistical significance using one-way ANOVA followed by Dunnett's multiple comparisons test.

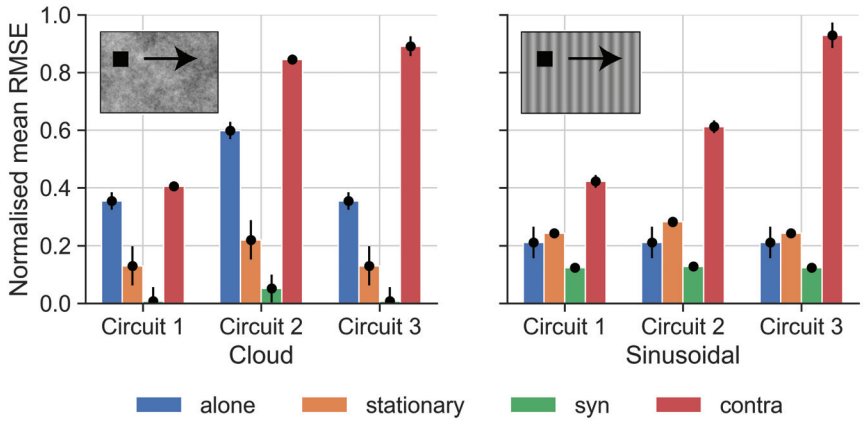


**Fig 8. Errors from fitting candidate circuits to biological TSDN data for cloud and sinusoidal backgrounds.** The normalised mean RMSEs from fitting each circuit described in Fig 4 to TSDN electrophysiological data (mean RMSE) for each condition for the cloud (left) and sinusoidal (right) backgrounds. The RMSEs of each circuit per condition are normalised by the equivalent RMSE of the 'STMD only' circuit. The whiskers of the black points indicate the standard deviation of the normalised mean RMSE of the particular bar plot.

i.e. same starting points of the target, as in electrophysiology, and took each neuron's receptive field (see Methods for details) into account in the simulations. Again, the errors between the biological and modelled TSDNs were quantified by a mean RMSE per neuron.

We found that the circuit 1 errors for the cloud and sinusoidal backgrounds were fairly consistent with those for the starfield background (compare Fig 6 and Fig 8). However, circuits 2 and 3 produced much higher errors (Fig 8) compared to those obtained on the starfield background, especially for contra-directional background motion. For circuit 2, this might be due to the 'overshooting' characteristic of the circuit (see e.g. Fig 5), which resulted in outputs much higher than the biological TSDN responses (Fig 8). For circuit 3, the large errors stemmed from the lack of target-like objects in the background, and the circuit's subsequent failure to produce facilitation. All three circuits struggled to have low errors to syn-directional motion for the sinusoidal background (Fig 8). This is because for 'syn'-directional motion, while the activities of all the circuits saturated to zero, the biological data (Fig 7J) indicates that some TSDN recordings did not exhibit much suppression, resulting in model testing errors. Taken together (Fig 7 and Fig 8), these results suggest that circuit 3 can be discounted as a viable TSDN circuit.

### Circuit 1 provides best fit to results of preceding optic flow experiments

Nicholas and Nordström [11] explored whether the TSDN response would also be affected by background motion that immediately preceded, but did not coincide with target motion. The stimuli consisted of two parts: (1) a preceding optic flow – background motion **before** target motion, and (2) concurrent optic flow – background motion **while** the target is in motion. Those experiments showed that the TSDN response was suppressed by preceding background motion if it was syn-directional to the subsequent target motion, even if there was no concurrent background motion. However, if the preceding background motion was contra-directional to the subsequent target

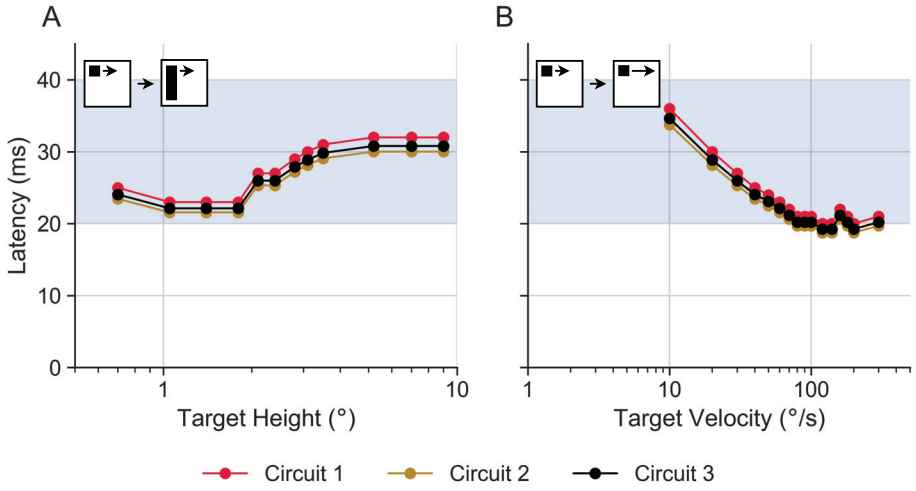


**Fig 9. Our TSDN model latencies exhibit similar latencies to biological TSDNs.** TSDN model latencies (red, circuit 1; yellow, circuit 2; black, circuit 3) to changing spatiotemporal target characteristics. (**A**) Model latencies for different bar target heights (fixed width of 0.8°, moving at 50°/s). Bar heights are in the range of 0.7−9°. (**B**) Model latencies for different velocities of square targets of fixed size 0.8°×0.8°. The velocity range is from 10−300°/s. The shaded region (20−40 ms) signifies the latency range observed in dragonfly TSDNs [27].

motion, no corresponding facilitation was observed [11]. An example stimulus consisting of contra-directional preceding (rightward motion) and stationary concurrent optic flow with a leftward moving target is presented in S1 Video. Here we used similar stimuli to discern how well circuits 1 and 2 match the biological TSDNs.

To understand how the timing of the stimuli affects the modelled circuits, we investigate the latency, which we define as the time between the onset of a stimulus and an elicited TSDN response $\geq 1$ Hz. Dragonfly TSDNs have latencies between 20 ms and 40 ms [27] and, for the relevant target heights and velocities (see Fig 3), all three TSDN model circuits exhibited latencies in this range (Shaded area, Fig 9). Thus, assuming that hoverfly TSDNs have latencies within a similar range as dragonflies, all three TSDN circuits capture this.

For the preceding optic flow experiments, Fig 10 shows the average TSDN response throughout the 0.48 s period of target motion, averaged across neurons and conditions; and normalised against the average TSDN response to a target moving 'alone' (data from [11]). In our simulations, the background was always stationary during target motion. In contrast, the preceding optic flow is either 'stationary', 'syn'- or 'contra'-directional. Fig 10 shows that circuit 1 reproduces experimental results in all three conditions. However, circuit 2 produces significantly different results to biological TSDNs for 'syn'-directional preceding optic flow (one-way ANOVA, followed by a post-hoc two-sample $t$-test with Bonferroni correction, $P \leq 0.0001$).

When excitatory preceding optic flow stops, LPTC activity decays back to the spontaneous rate, with a time constant similar to the response onset (*left*, Fig 2). Vice versa, when inhibitory preceding optic flow stops, LPTC activity rises to the spontaneous rate. While circuit 1 receives input from one LPTC, circuit 2 receives input from two LPTCs, with opposite preferred directions of motion (equations of circuits in Fig 4). As such, in circuit 2, this opposing LPTC activity results in lower suppression of

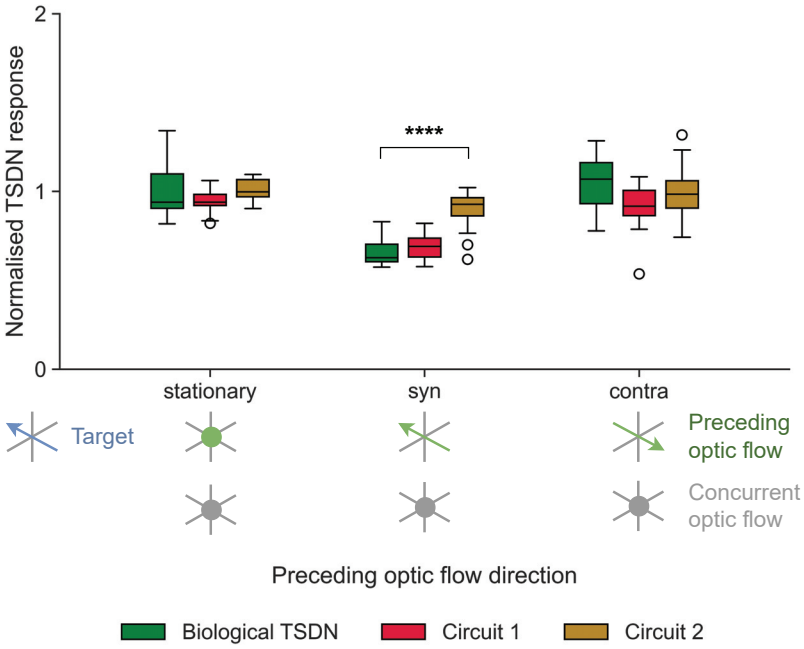


**Fig 10. Model and biological TSDN outputs to preceding optic flow.** The outputs of the fitted circuits compared with biological TSDN data [11] for the preceding optic flow experiments. In the legend, different visual stimuli are colour-coded: target (blue), preceding optic flow (green) and concurrent optic flow (grey). If the background is stationary, the optic flow is denoted by a dot. The box edges denote the first and third quartiles of the data, with a line at the median. The whiskers denote the furthest data point within 1.5x the interquartile range (IQR). The non-filled circles are outliers. Significance is shown with one-way ANOVA followed by two-sample $t$-tests with Bonferroni correction (****$P \leq 0.0001$).

the TSDN response to syn-directional preceding optic flow (Fig 10).

While the LPTC model has a decay time constant of 40 ms (Fig 13), all the TSDN circuit models exhibit a latency of ∼20 ms (Fig 9). Therefore, for the preceding optic flow to have any effect on TSDN output, the target has to be within the TSDN receptive field while the LPTC activity is still decaying back to its spontaneous rate. Otherwise, the TSDN response will not be affected by the preceding background motion.

Interestingly, while in the preceding optic flow tests, circuit 2 does not provide adequate TSDN response suppression to 'syn'-directional background motion, in the 'error fitting' experiments (Fig 6), circuit 2 adequately suppresses the TSDN response to 'syn'-directional optic flow. This is because, in the 'error fitting' experiments, the 'syn'-directional background motion continued even during target motion, and as such, the LPTC activity did not return to its spontaneous rate until after the target motion stopped. Therefore, the TSDN response was fully suppressed during target motion.

### Circuit 1 provides best fit to results of dot density experiments

In all previous experiments, the density of the starfield background was kept at 100 dots/m$^3$. However, Nicholas and Nordström [11] previously explored whether varying the dot density from $10 - 500$ dots/m$^3$ affected the background modulation of the TSDN response. While they found that TSDN responses were not facilitated when background motion was contra-directional to target motion at low dot densities, they were facilitated at high dot densities. In contrast, TSDN responses were suppressed when background motion was syn-directional across all dot densities tested. An example stimulus of the starfield background with a dot density of 500 dots/m$^3$ moving contra-directional to a leftward moving target is presented in S2 Video.

Fig 11 shows the normalised model and biological TSDN responses to a target moving against stationary, syn- and contra-directional background motion, across various dot densities. Both circuits reproduce the suppression observed in biology (middle row, Fig 11). While circuits 1 and 2 sometimes exhibit suppression significantly stronger than biology, these happen in instances where biology showed large variation (middle densities, middle row, Fig 11).

However, when it comes to facilitation, which depended on dot density in biology [11], circuit 2 sometimes produces TSDN outputs that are significantly different (asterisks in Fig 11). Circuit 2 performs comparatively poorly because the amplification of the STMD activity by the LPTC with the opposite preferred direction (purple arrow, Fig 4) results in TSDN responses that *overshoot* the biological TSDN responses (see e.g. Fig 5). Interestingly, for contra-directional motion at 10 dots/m$^3$, while circuit 2 outputs show facilitation, circuit 1 outputs match biological TSDN responses in exhibiting no facilitation (bottom row, Fig 11).

Our model suggests that, at a dot density of 10 dots/m$^3$ where the LPTC activity is low, there will be low/no facilitation of TSDN responses by contra-directional background motion. However, since even at a low dot density, syn-directional motion causes suppression of TSDN responses (middle row of Fig 11; [11]), this would indicate that the LPTC synaptic weight would have to be quite high relative to the STMD synaptic weight to fully suppress the STMD activity. This is confirmed in the LPTC synaptic weight ($\beta$) hyperparameter values obtained for both circuits 1 and 2 (shown in Table 1). Taken together, these last two experiments (Fig 10 and Fig 11) suggest that circuit 1 is the most biologically plausible circuit.

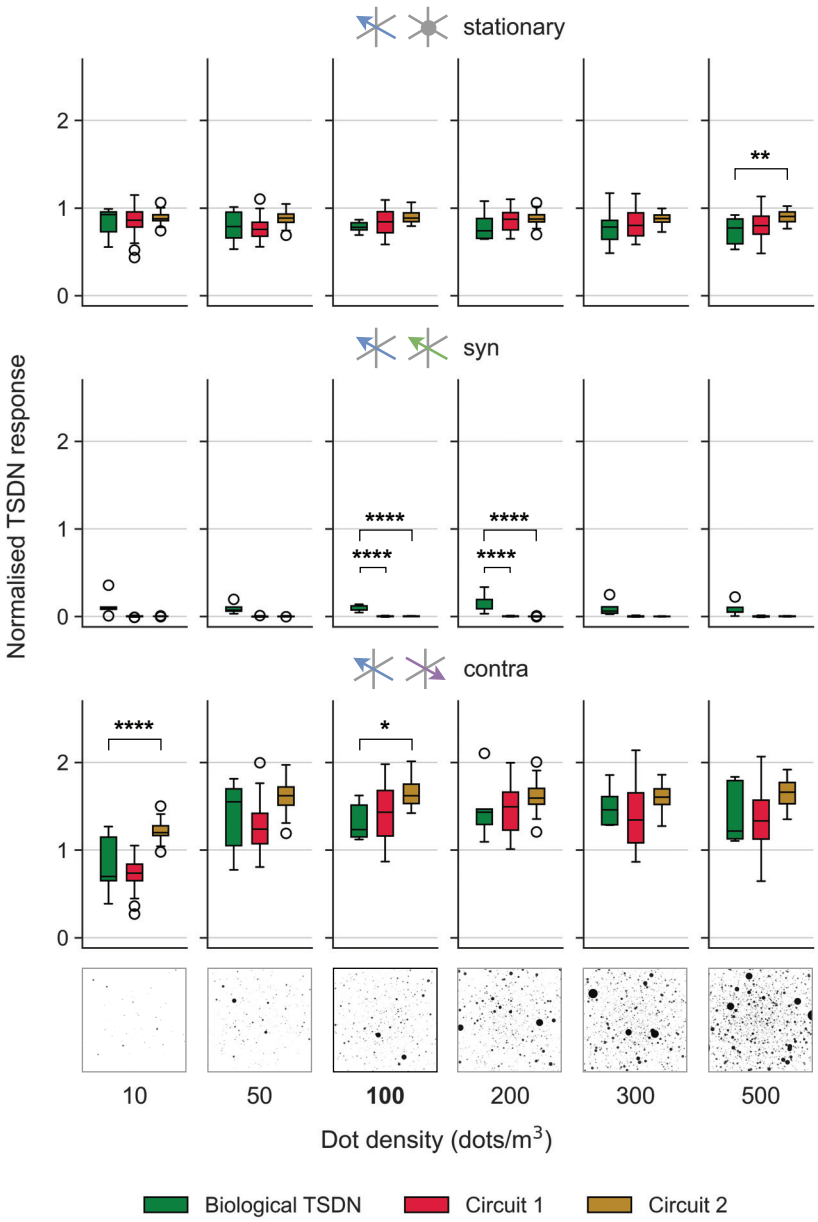


**Fig 11. Model and biological TSDN outputs of dot density experiments.** The outputs of the fitted circuits and biological TSDN data (from ref [11]) for the starfield background with variable dot density. The different motion directions are colour-coded and results are laid out as such: target (blue), stationary (grey; top row), syn- (green; middle row) and contra-directional (purple; bottom row). The directions of the arrows indicate the direction of motion. If the background is stationary, this is denoted by a dot. The default starfield background at 100 dots/m$^3$ is highlighted in bold. In each grid, significance is shown with one-way ANOVA followed by two-sample $t$-test with Bonferroni correction (*$P \leq 0.05$, **$P \leq 0.01$, ***$P \leq 0.001$, ****$P \leq 0.0001$).

# Discussion

We modelled three candidate TSDN circuits (Fig 4) using STMD and LPTC input to provide the suppression by syn-directional motion and the facilitation by contra-directional motion seen in biology (Fig 7). Our candidate TSDN circuits were based on plausible combinations of existing STMD [16] and LPTC [13] models. We fitted our circuit models to published data [11], and then used new electrophysiology data to rule out one of the circuits (Fig 7; Fig 8). Then, we compared the remaining circuits against published preceding optic flow (Fig 10) and dot density data (Fig 11) [11]. Through the interplay of STMD and LPTC dynamics, our best-fitting model (circuit 1) provides mechanistic explanations for suppression/facilitation of TSDN responses in the presence of syn- and contra-directional background motion, as well as observations related to preceding optic flow and dot density experiments [11].

While our deterministic model can predict how an *average* TSDN might respond to different target and background combinations, our model cannot explain the large variability seen between TSDNs (inter-neuronal variability), seen in Figs 7H-J, nor the variability between repetitions of the same stimulus and neuron (inter-trial variability) present in the extracellular TSDN recordings (Fig 1 of [11]). This variability could be explained by numerous factors: Varying strengths of connections between neurons [28] could lead to inter-neuron variability in TSDN responses. Furthermore, due to the nature of our backgrounds (Fig 7), there are localised patches of high and low brightness. Therefore, if the black target moved over a dark region of the background, it would have lower contrast and thus generate lower STMD activity (Fig 6 of [16]). However, after examining the exact backgrounds and target positions used, we did not find sufficient evidence to support the differences in background as a prominent cause of inter-neuronal variability (data not shown). Another source of variability could be local changes in directional selectivity within a TSDN receptive field (Fig 1 of [1]). Again, we did not find sufficient evidence that this is a primary cause of inter-neuronal variability (data not shown). Furthermore, hoverflies, like dragonflies, are poikilothermic animals with limited thermoregulation. Temperature has been shown to have a significant impact on the tuning properties of dragonfly STMD neurons [29], suggesting that any variations in temperature during recording sessions could lead to inter-trial variability. Finally, in blowflies, the response characteristics of LPTCs have been shown to depend on the activity state of the animal, i.e. LPTCs have different response characteristics depending on whether the animal is stationary, walking or flying [30]. This state dependence can be mimicked by the application of chlordimeform (CDM, an octopamine receptor agonist). CDM has been shown to affect hoverfly LPTCs [31]. Thus, it is plausible that activity- or attention-based LPTC modulation could contribute to inter-trial variability.

Leading with the hypothesis that physiological or motivational state, e.g. temperature and locomotor state, change the effective 'synaptic weights' leading to the observed variability, we scale both the STMD and LPTC synaptic weights ($\alpha$ and $\beta$) in our model to simulate variability (data not shown). Scaling $\alpha$ leads to varying excitatory input to the TSDN, such that when $\alpha$ tends to zero, the circuit resolves to the LPTC response, thus the TSDN output tends to zero. In contrast, a very large $\alpha$ could make our circuit 1's TSDN output match the 'STMD only' circuit, which does not exhibit facilitation/suppression (see e.g. blue data, Fig 5). Changing $\beta$ in contra-directional background-motion instances leads to the TSDN output being amplified, resulting in higher facilitation, consistent with experimental data showing extremely large TSDN facilitation (Fig 7). Conversely, in syn-directional optic flow instances, the TSDN output is driven to zero more strongly (TSDN output must be non-negative). Both 'alone' and 'stationary' TSDN outputs are unaffected by scaling $\beta$.

In hoverflies, TSDNs are believed to play a role in target pursuit and provide input

to motor neurons [6]. In fact, recent studies in dragonflies have suggested that TSDNs may drive foveating head movements that stabilise the target image on the eye before and probably throughout the interception flight [32]. Interestingly, in response to target images reconstructed from pursuits [5], hoverfly TSDNs do not respond strongly [1]. However, these were not completely natural as the hoverflies were pursuing artificial targets in a free flight arena [5]. In nature, male *Eristalis* hoverflies set up territories, which they defend vigorously against other insects [33]. As they typically initially detect these intruding insects from a stationary stance, this would resemble our 'stationary' conditions. However, once pursuit is initiated, the background patterns would resemble our 'syn' and 'contra' conditions. In the future, it would be interesting to reconstruct both target images and optic flow generated during such target pursuit to determine how often the background moves 'syn'- and 'contra'-directional to the target. This would help evaluate the ecological impact of our findings.

# Materials and methods

## STMD modelling

Our STMD model implementation (Fig 12) can be partitioned into four stages: (1) 'Early visual processing', which includes the temporal and spatial filtering found in fly optics, photoreceptors and lamina monopolar cells; (2) 'Target matched filtering' which includes the processes that lead to the discrimination of the target against visual clutter; (3) 'Directional selectivity' which makes the resultant ESTMD directionally selective; (4) 'Receptive fields' to match the modelled STMD to that of a biological small-field STMD [20].

For stages (1-2) we reproduced the ESTMD model presented by Wiederman et al. [16] and Bagheri et al. [21]. We here added stages (3-4), providing directional selectivity and small-field STMD receptive fields. We also tuned our ESTMD model hyperparameters to match hoverfly physiology. Details about the STMD model implementation are in the Supplementary section.

### Directional-selectivity

Since TSDNs are directionally selective [1], even in the absence of widefield motion, and based on our hypothesis that STMDs primarily drive the target selectivity seen in TSDNs, input from directional model STMDs seems plausible. To implement this, the non-directionally-selective ESTMD outputs are passed through a two-point correlator, namely a Hassenstein-Reichardt Elementary Motion Detector (HR-EMD) [14], resulting in a preferred and an anti-preferred direction of target motion. As illustrated in Fig 13A, in the HR-EMD mechanism, two spatially segregated inputs ($x_1$ and $x_2$), separated by distance $\phi$, are correlated ($\times$) after delaying (D) one of the signals. The delay operator, D is the same as used in Eq 11 with a time constant, $\tau_D$ ($\tau_D = 40\,\text{ms}$). The correlation outputs are then subtracted, resulting in an HR-EMD output that gives positive output to one direction of motion, and negative output to the other.

The ESTMD output from 'target matched filtering' can be represented as a 2D matrix (*Top*, Fig 13B). Spatially segregating this matrix by a distance $\phi$, the spatially segregated inputs to the HR-EMD can be obtained. In this case, the green and purple shaded regions become $x_1$ and $x_2$ respectively (as described in Fig 13A). Finally, the HR-EMD output is passed through a Rectified Linear Unit (ReLU) block so that the output is non-negative.

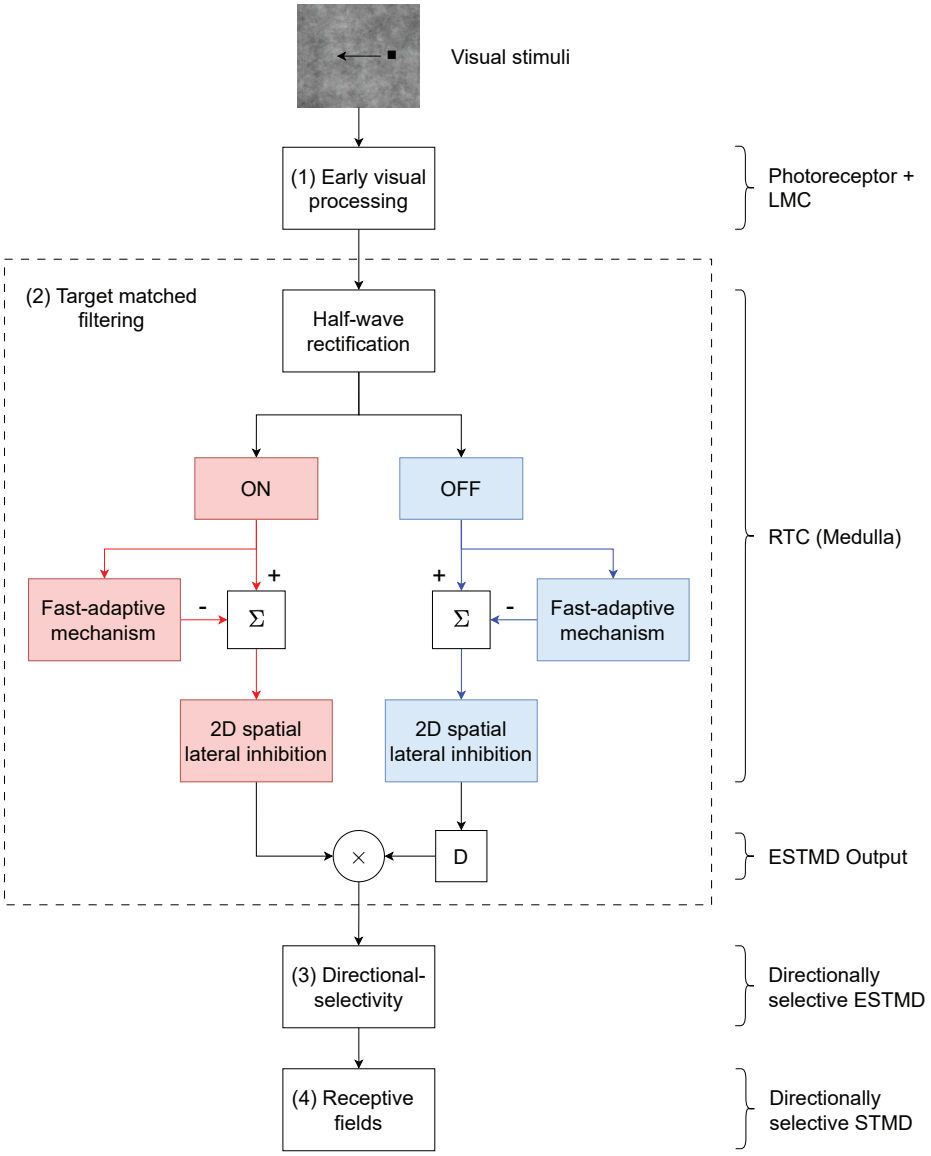


**Fig 12. STMD model.** Our STMD implementation – based on Wiederman et al. [16] with our additions to create directional selectivity and mimic STMD receptive fields. Visual stimuli first undergo early visual processing in the fly photoreceptors and lamina monopolar cells (LMC). The LMC output is then separated into ON (red) and OFF (blue) channels which are independently processed through rectifying transient cells (RTCs) found in the fly medulla. Then, the ESTMD output is a single-point correlation of a delayed OFF signal with an undelayed ON signal, as in [16, 21]. The ESTMD output is then made directionally selective and spatially pooled using a 2D Gaussian representative of a small-field STMD's receptive field [20].

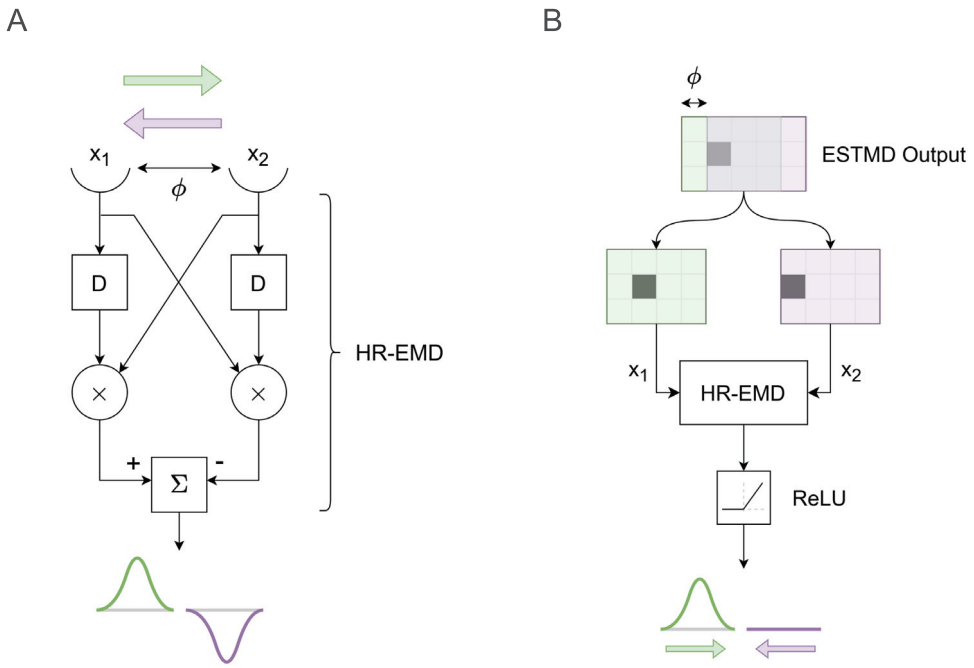


**Fig 13. HR-EMD mechanism leads to directional ESTMD output.** (**A**) The Hassenstein Recichard-EMD mechanism detects directional motion, here rightwards or leftwards motion (green or purple arrows) and produces a positive or negative response, denoted by a Gaussian, corresponding to the preferred (green) or anti-preferred (purple) direction. (**B**) The ESTMD output, represented as a 2D matrix, is split into two spatially segregated channels (green and purple matrices) that feed into the HR-EMD mechanism described in (A). The output is then half-wave rectified. In this case, the preferred direction of target motion is rightwards (green).

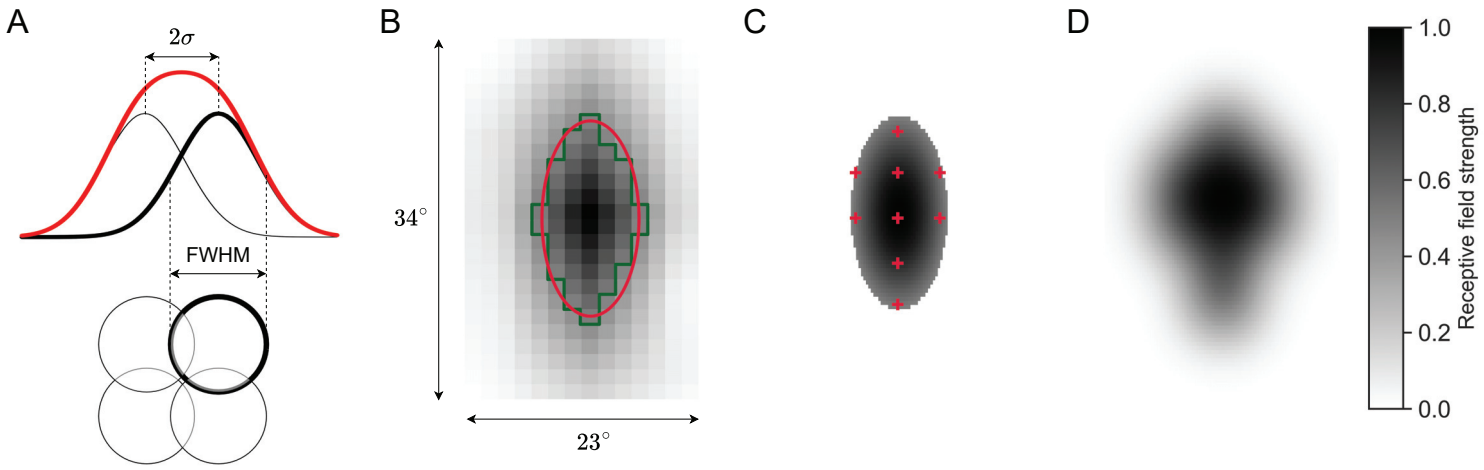


**Fig 14. Constructing STMD receptive fields.** (**A**) *Top*. The small-field STMD receptive field [20] is modelled as a Gaussian, shown in black. The distance between the centres of two adjacent receptive fields is then $2\sigma$, where $\sigma$ is the standard deviation of the Gaussian. Due to the Gaussians overlapping, the effective STMD receptive field strength is obtained through superposing (linear summating) the Gaussians. The superposed STMD receptive field is shown in red. *Below*. The STMD receptive fields at 50% maximum (full width at half maximum; FWHM), shown as circles, are arranged in a square grid. A model STMD receptive field and associated Gaussian are highlighted for clarity. (**B**) A $34° \times 23°$ cropped patch of the visual field highlighting an example biological TSDN receptive field. The contours at 50% receptive field strength of the mapped TSDN receptive field (green) and a fitted 2D Gaussian (red). (**C**) The centres of the STMD receptive fields (red plusses) needed to create the biological TSDN receptive field in panel B are here overlayed on the 2D Gaussian. (**D**) The resulting modelled TSDN receptive field reconstructed from the superposed STMD receptive fields shown in panel C.

### TSDN Receptive fields

The final STMD output is obtained by spatially pooling directionally-selective ESTMD outputs (stage 3 in Fig 12). Barnett et al. [20] found that hoverfly small-field STMD receptive fields can be roughly expressed as a 2D isotropic Gaussian with $\sigma = 3°$. Thus, to achieve a good match with hoverfly biology, each STMD pools its inputs from a 2D Gaussian with $\sigma = 3°$. The receptive fields of multiple STMDs then tile the visual field with their centres separated by $2\sigma$ [34, 35], resulting in a small overlap as shown in Fig 14A.

The receptive field mapping method for biological TSDNs described in Nicholas and Nordström [11] leads to a coarse TSDN receptive field, shown with a green outline in Fig 14B. To improve the spatial resolution of the TSDN receptive field to a degree suitable for the modelling, we fitted 2D Gaussians to the coarse biological TSDN receptive fields, shown with a red outline in Fig 14B. Since we presume that STMDs are presynaptic to TSDNs, to ensure the model is TSDN receptive field-size invariant, we reconstructed the TSDN receptive field from model STMD receptive fields. In this way, since the receptive fields of small-field STMDs are smaller than those of TSDNs, multiple STMD outputs pool to give a single TSDN output. To calculate the number and locations of STMDs comprising each TSDN, we correlated the tiled STMDs across the visual field with the location of the TSDN receptive field (using the 50% Gaussian). In Fig 14C, the resultant STMD centres are shown as red plusses. Thus, by superposing the outstanding model STMD receptive fields, a reconstructed model TSDN receptive field was achieved (Fig 14D).

The widefield STMD used in circuit 3 (Fig 4) was modelled in a similar way to the small-field STMD. However, the large-field STMD spans over an azimuthal range of $0 - 30°$ and an elevation from $30 - 69°$ (the upper bound of the visual field) ipsilateral to the TSDN receptive field [10].

### Lobula Plate Tangential Cell (LPTC) modelling

Optic-flow sensitive neurons in the fly optic lobe are known as Lobula Plate Tangential Cells (LPTCs). LPTCs integrate local motion signals from small-field T4 and T5 neurons [36]. In the absence of motion, spiking LPTCs fire at a spontaneous (baseline) rate and their activity increases or decreases from this baseline, depending on whether widefield motion is in the preferred direction (PD) or null direction (ND). However, the change in LPTC activity to widefield motion is asymmetric and dependent on the direction of the widefield motion [37] i.e. the increase in LPTC activity is proportionally higher than the decrease in LPTC activity for the same amount of widefield motion in the preferred and null directions respectively (Fig 1).

Using inputs from two spatially-segregated points, we passed each ON-ON and OFF-OFF combination of inputs through a 2-quadrant-detector [38], to obtain two EMD outputs – one that has a PD to the right and another to the left (green and purple respectively in Fig 15). Each EMD output is half-wave rectified and spatially pooled. Spatial pooling creates a uniform directionally selective LPTC receptive field spanning across all elevations to either side of the azimuthal midline e.g. left side of the visual field has LPTC with preferred direction to the left. The resultant ND response is multiplied by a ratio, $\gamma$ before subtracting from the resultant PD response (Fig 15) to provide an LPTC output. This linear subtraction imbues the LPTC output with an asymmetric sensitivity to widefield motion.

$\gamma$ (Fig 15A) is defined as the ratio of maximum increment to maximum decrement of the LPTC response about the spontaneous rate. The functional equation of the LPTC model involves the linear subtracted output (encompassed in curly brackets, Fig 15B) being scaled by a scaling coefficient, $g$, before being added to a non-zero spontaneous

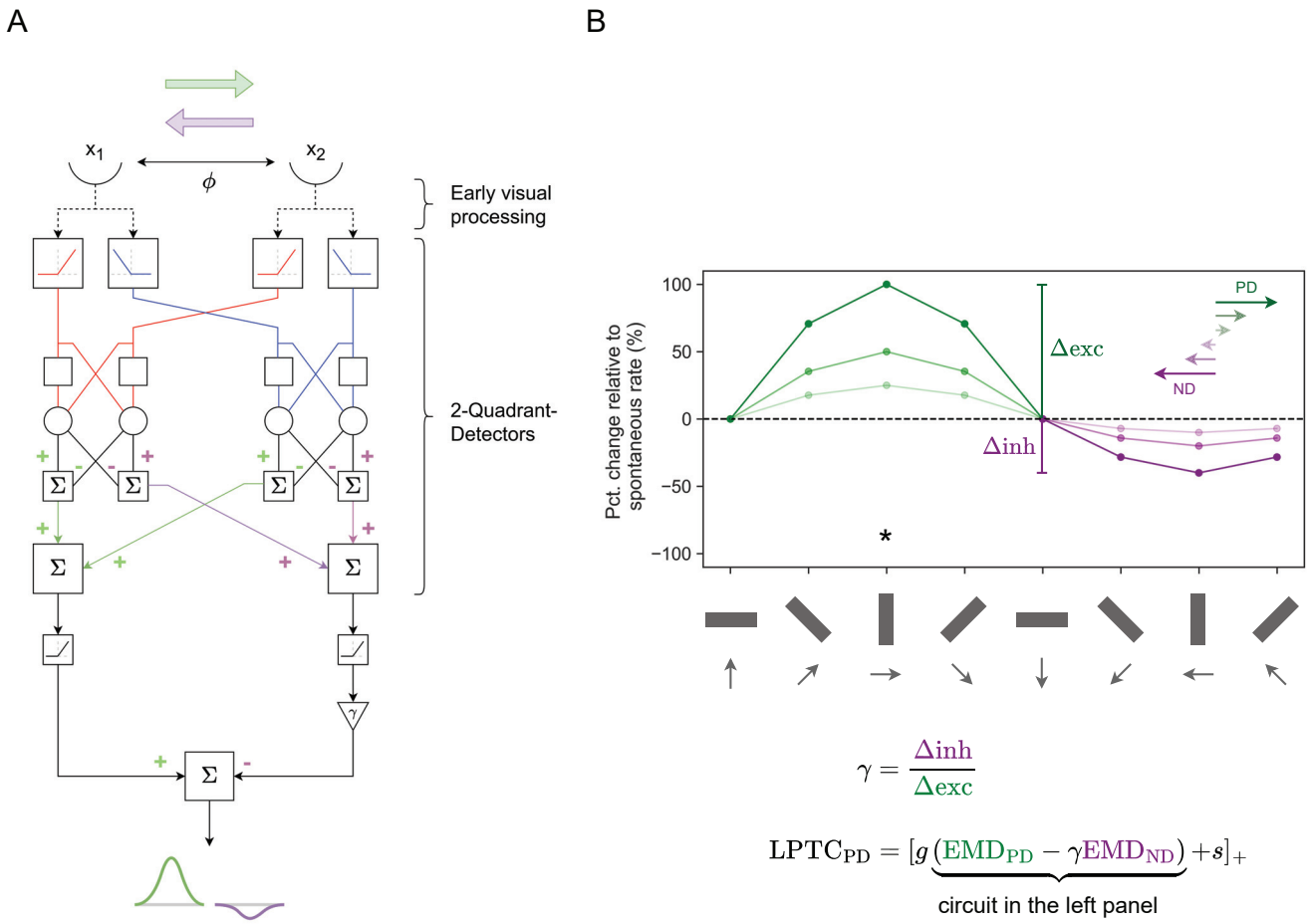


**Fig 15. LPTC modelling** (**A**) The inputs from two spatially-segregated points ($x_1$ and $x_2$) first undergo the same 'early visual processing' as the STMD model (Fig 12). Using 2-quadrant-detectors where only input combinations of the same contrast polarity are processed (ON-ON, OFF-OFF), directionally selective EMDs in the preferred direction (PD, green) and null direction (ND, purple) are obtained. In this case, the PD is to the right and ND to the left. The structural motifs in this circuit are the same as those in Fig 13A. (**B**) The direction sensitivity and the effect of different velocities of motion (longer and darker arrows denote higher velocity) in the PD and the ND on the modelled response. The grey arrows denote the direction of motion of the bar. In this case, the PD of motion is to the right, denoted by the *.

rate, $s$. The LPTC model response is clamped at zero as the spiking frequency cannot be negative.

## Electrophysiology

Male *Eristalis tenax* hoverflies were immobilised at room temperature ventral side up using a mixture of beeswax and resin. A small region of the cuticle was removed at the anterior end of the thorax to expose the cervical connective. A fine wire hook was placed under the cervical connective for mechanical support and a silver wire was inserted into the cavity as a reference electrode.

Extracellular recordings were made from the cervical connective using a sharp polyimide-insulated tungsten microelectrode (2 MΩ; Microprobes). Data were amplified at 100 gain and filtered through a 10−3000 Hz bandwidth filter using a DAM50 differential amplifier (World Precision Instruments), with 50 Hz noise removed with a Hum Bug (Quest Scientific). Data were acquired and digitised at 40 kHz using Powerlab 4/30 and LabChart 7 Pro (ADInstruments). Single units were discriminated by amplitude and half-width using Spike Histogram software (ADInstruments).

During the experiment, hoverflies were positioned perpendicular to and 6.5 cm away from the middle of a linearised LCD screen (ASUS) with a mean illuminance of 200 lx, a refresh rate of 165 Hz, and a spatial resolution of $2560 \times 1440$ pixels ($59.5 \times 33.5$ cm), giving a projected screen size of $155° \times 138°$. Visual stimuli were displayed using custom software written [39] in MATLAB (version R2019b; MathWorks) using the Psychophysics toolbox [40, 41].

TSDNs were identified as described [9]. In short, we mapped the receptive field of each neuron by scanning a target horizontally and vertically at 20 evenly spaced elevations and azimuths [1] to calculate the local motion sensitivity and local preferred direction. We then scanned targets of varying height through the small, dorso–frontal receptive fields to confirm that each neuron was sharply size tuned with a peak response to targets subtending 3° to 6°, with no response to larger bars, to looming or widefield stimuli [1, 9].

## Visual stimuli

To test the effects of background motion on the TSDN response, we displayed targets against one of four different backgrounds (shown in Fig 16). Unless otherwise mentioned, targets were black and round with a diameter of 15 pixels (starfield background) or $15 \times 15$ pixels black squares (cloud and sinusoidal backgrounds), moving at a velocity of 900 pixels/s for 0.48 s. When converted to angular values and taking the small frontal TSDN receptive fields into account [1], this corresponds to an average diameter of 3° and a velocity of 130°/s [24]. Unless otherwise stated, each target travelled in each neuron's preferred horizontal direction (i.e., left or right) and across the centre of its receptive field. The target elevation was varied slightly between repetitions to minimise habituation [11]. There was a minimum of 4 s between each stimulus presentation.

The background stimuli all covered the entire visual monitor, i.e. they had a spatial extent of $2560 \times 1440$ pixels, corresponding to $155° \times 138°$ [11]:

**Starfield** a 2D rendering of a simulated 3D environment containing randomly located spheres. These were perspective corrected to display the optic flow that would be generated if the hoverfly was sideslipping at 50 cm/s, with size and greyscale indicating their relative distance from the hoverfly (see ref [25] for more details). Some of the spheres had the same spatio-temporal characteristics as the target.

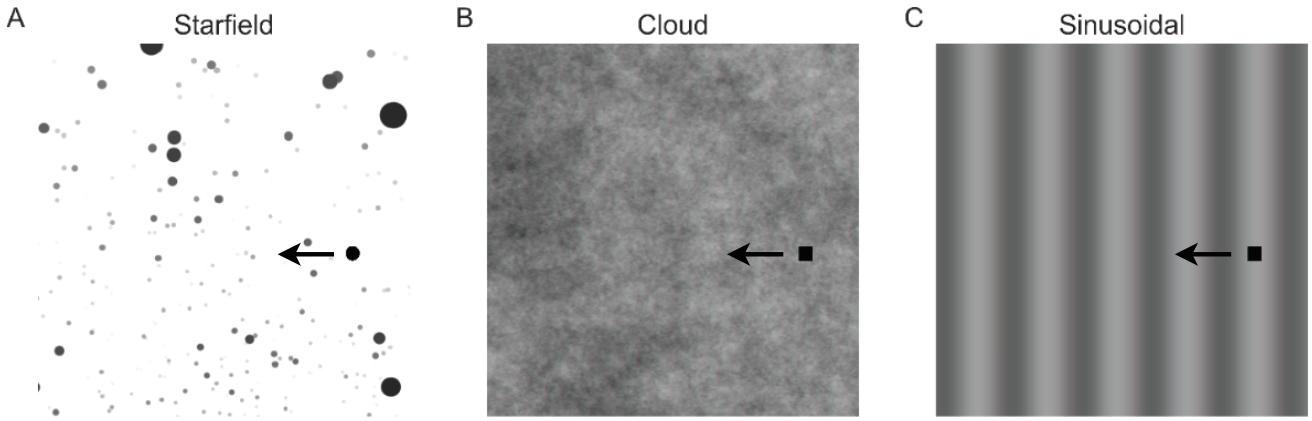


**Fig 16. Target-background combinations.** The three background stimuli used for both electrophysiology and simulations: (**A**) Starfield, (**B**) Cloud, (**C**) Sinusoidal. The target for the background in (**A**) was 15 pixels diameter black dots moving at 900 pixels/s. The targets for the backgrounds in (**B,C**) were 15 pixels side length black squares moving at 900 pixels/s. The targets traversed the background in the preferred direction of each TSDN – in this case, to the left.

**Cloud** a greyscale background with a 2D power spectrum similar to that of typical natural scenes and a mean luminance of $\sim 128$ where luminance $\in [0, 255]$ [24] with a Michelson contrast of 100% (see ref [7] for more details).

**Sinusoidal** a vertical sinusoidal grating with an average wavelength of 7°, drifting at 5 Hz, and a Michelson contrast of 25%.

For each background, four conditions were tested. (1) 'alone': the target moved across a homogeneous white (starfield) or grey (cloud and sinusoidal) background; (2) 'stationary': the target moved over a non-moving background; (3) 'syn'-directional: the target moved in the same direction as the background; (4) 'contra'-directional: the target moved in the opposite direction to the background. TSDN responses from a single TSDN neuron exposed to the 'cloud' background are illustrated in Fig 7. The same stimuli shown to the hoverflies were also presented to the model as a sequence of images, each presented for 1 ms.

## Obtaining TSDN spike rates

The extracellular recordings of the TSDN experiments yielded spike trains. To allow these to be compared with the output of our rate-based model, we convolved the spike trains with Gaussian kernels to obtain a Spike Density Function (SDF):

$$s(t) = \sum_i \kappa(t - t_i) \tag{1}$$

$$\kappa(t) = \frac{1}{\sigma\sqrt{2\pi}} \exp\left(-\frac{t^2}{2\sigma^2}\right) \tag{2}$$

where $t_i$ are the times of individual spike and $\sigma = 20$ ms is the standard deviation of the Gaussian kernel $\kappa$.

## Data Analysis and Statistics

We recorded from 10 TSDNs (cloud) and 6 TSDNs (sinusoidal) in 16 male hoverflies. We kept data from all TSDNs that showed a robust response to a target moving over a white background. We repeated this control throughout the recording and only kept data from neurons that responded consistently. We only kept data from experiments with a minimum of 12 repetitions. The data from repetitions within a neuron were converted to rates (see above) and averaged per condition. We normalised the responses to each neuron's own mean response to a target moving over a white or grey background.

Data analysis of electrophysiology data was performed in Matlab. Throughout the paper, n refers to the number of repetitions within one neuron and N to the number of neurons. The sample size, type of test, and $P$ value are indicated in the corresponding figure legends. For the cloud and sinusoidal electrophysiological recordings (Fig 7), paired $t$-tests or one-way ANOVAs, followed by Dunnett's post hoc test for multiple comparisons were used (using Prism 10.4.1 for Mac OS X (GraphPad Software)). For the preceding optic flow (Fig 10; S1 Video) and dot density results (Fig 11; S2 Video), one-way ANOVA followed by two-sample $t$-tests with Bonferroni correction for multiple comparisons was used.

## Data and code availability

Electrophysiology data has been deposited on Figshare `https://figshare.com/s/c1d9631df02f4ea4637b`. The code is available on GitHub `https://github.com/anindyaghosh/STMD/tree/Photoreceptors`. These are temporary links for the review process.

# Supporting information

### S1 Supplementary. Implementation details of the STMD model.

#### Early visual processing

Similarly to Wiederman et al. [16], our ESTMD model only used the green channel of the RGB image input – this is an approximation of the green spectral sensitivity of the movement detection mechanisms in hoverflies [42]. The tiny lenses of compound eyes cause diffraction of light [43], which results in reduced spatial acuity, i.e. high optical blur. Following Wiederman et al. [16], we modelled this optical blur by convolving a circularly symmetric 2D Gaussian kernel with the stimulus image,

$$G(x, y) = \frac{1}{2\pi\sigma^2} \exp\left(-\frac{(x^2 + y^2)}{2\sigma^2}\right) \tag{3}$$

where $\sigma$ is the standard deviation. In order to emulate the hoverfly optics [44], we calculated $\sigma$ through the full-width at half maximum (FWHM) of the fly optical angular sensitivity, which is 1.4° [43]. Therefore, $\sigma$ can be calculated in pixels as:

$$\sigma = \frac{1.4}{2\sqrt{2\ln 2}} \times \text{pixels/degree} \approx 9.8 \text{ pixels} \tag{4}$$

where pixels/degree = 2560/158 is calculated by dividing the spatial resolution of the visual stimulus by the subtended viewing angle of the visual field of the hoverfly eye, based on an inter-ommatidial angle of 1° [44]. This consideration is also applied next for the spatial downsampling of the blurred image where each pixel represents a degree of

**Table 2.** Coefficients of the discrete DLN function shown in Eq 5.

| Numerator coefficients | | Denominator coefficients | |
|---|---|---|---|
| $\alpha_1$ | $-0.15240$ | $\beta_1$ | $0.06510$ |
| $\alpha_2$ | $0.17890$ | $\beta_2$ | $-0.54180$ |
| $\alpha_3$ | $-0.05700$ | $\beta_3$ | $2.14480$ |
| $\alpha_4$ | $0.04300$ | $\beta_4$ | $-5.30600$ |
| $\alpha_5$ | $-0.01600$ | $\beta_5$ | $9.00040$ |
| $\alpha_6$ | $0.00440$ | $\beta_6$ | $-10.71100$ |
| $\alpha_7$ | $-0.00076$ | $\beta_7$ | $8.68500$ |
| $\alpha_8$ | $0.00006$ | $\beta_8$ | $-4.33300$ |

the visual field. The kernel size of the discrete Gaussian approximation is determined as $2\lceil 3\sigma \rceil) - 1 = 61$ pixels, as opposed to the kernel size determination used by Bagheri et al. [21] which gives $2\lceil \sigma \rceil = 20$ pixels. Our choice of kernel size results in a discrete kernel that includes the $99^{th}$ percentile of the Gaussian while the odd size mitigates aliasing.

Next, the Lamina Monopolar Cells (LMCs) remove redundant information by using neuronal adaptation (temporal high-pass filtering) and centre-surround antagonism (spatial high-pass filtering). Wiederman et al. [16] modelled this using a Lipetz transform. Since the temporal filtering qualities of both the photoreceptors and LMC can be combined to give a temporal band-pass filter [21], for simplicity, we used such a filter instead. This filter was approximated and simulated using a discrete transfer function of a difference of log-normals (DLN) as per the method described by Halupka et al. [45]:

$$y[n] = \sum_{i=1}^{8} \alpha_i x[n + (i - 9)] - \sum_{i=1}^{8} \beta_i y[n + (i - 9)] \tag{5}$$

where $x[n]$ is the unfiltered signal and $y[n]$ the filtered output at a discrete timestep, $n$, and $\alpha_i$ and $\beta_i$ are the numerator and denominator coefficients given in Table 2.

Again, similar to [21], we applied centre-surround antagonism in the LMC by convolving the image with a zero-mean high-pass filter kernel $H$:

$$H = \frac{1}{9} \begin{bmatrix} -1 & -1 & -1 \\ -1 & 8 & -1 \\ -1 & -1 & -1 \end{bmatrix}$$

### Target matched filtering

Similar to [16, 21], the output from the LMC was first half-wave rectified and then separated into ON (brightness increments) and OFF (brightness decrements) contrast polarity channels:

$$\mathrm{I_{ON}}(y) = \begin{cases} y & \text{if } y > 0 \\ 0 & \textit{otherwise} \end{cases} \tag{6}$$

$$\mathrm{I_{OFF}}(y) = \begin{cases} -y & \text{if } y < 0 \\ 0 & \textit{otherwise} \end{cases} \tag{7}$$

where $y$ represents the output from the LMC at a discrete timestep and $I$ is the independent channel half-wave rectified output i.e. ON or OFF channel. Wiederman et al. [16] was inspired by the rectifying transient cells (RTCs) found in the blowfly medulla [46]. This fast-adaptive mechanism which 'adapts' the independent ON and OFF channels was also implemented in [21] and this work. Depending on whether the

independent channel signal is increasing or decreasing, the time constant of the nonlinear filter (NLF) used to implement this process switches [16]. The time constant is 'fast' ($\tau_{\text{fast}} = 10\,\text{ms}$) for an increasing signal or 'slow' ($\tau_{\text{slow}} = 100\,\text{ms}$) for a decreasing signal. Subsequently, for each polarity channel, at each discrete timestep, the channel NLF value is subtracted from the half-wave rectified channel signal. Through this subtraction, responses to the contrasting edges of visual features are enhanced, whilst lower-contrast 'textural details' are rejected. The NLF is computed through a temporal low-pass filter,

$$\text{NLF}[n] = (1 - \alpha[n]) \cdot I[n] + \alpha[n] \cdot \text{NLF}[n-1] \tag{8}$$

where $I[n]$ represents the independent channel signal at a certain discrete timestep $n$. The smoothing factor, $\alpha$ of the NLF is selected using the fast-adaptive mechanism described above:

$$\alpha[n] = \begin{cases} \exp\left(-T_s/\tau_{\text{fast}}\right) & \text{if } I[n] - I[n-1] > 0 \\ \exp\left(-T_s/\tau_{\text{slow}}\right) & \text{if } I[n] - I[n-1] \leq 0 \end{cases} \tag{9}$$

where $T_s$ is the sampling period ($T_s = 1\,\text{ms}$). While Wiederman et al. [16] used $\tau_{\text{fast}} = 1\,\text{ms}$, $\tau_{\text{slow}} = 100\,\text{ms}$ and Bagheri et al. [21] used $\tau_{\text{fast}} = 3\,\text{ms}$, $\tau_{\text{slow}} = 70\,\text{ms}$, we used $\tau_{\text{fast}} = 10\,\text{ms}$, $\tau_{\text{slow}} = 100\,\text{ms}$ as we found that these parameters led to ESTMD spatio-temporal tuning characteristics that better matched hoverfly physiology [10]. Similar to both [16, 21], the independently adapted ON and OFF channels were then convolved with a further centre-surround antagonistic kernel $H_{\text{inh}}$. This process represents the spatial lateral inhibitory effect within polarity channels seen in blowfly RTCs [47]. Target size tuning is achieved by varying the gain, $\gamma$ and spatial extent of the centre-surround antagonism described by the $H_{\text{inh}}$ kernel:

$$H_{\text{inh}} = \gamma \cdot \begin{bmatrix} -1 & -1 & -1 & -1 & -1 \\ -1 & 0 & 0 & 0 & -1 \\ -1 & 0 & 2 & 0 & -1 \\ -1 & 0 & 0 & 0 & -1 \\ -1 & -1 & -1 & -1 & -1 \end{bmatrix}. \tag{10}$$

While Wiederman et al. [16] accomplished spatial lateral antagonism by subtracting a temporally low-pass filtered signal of the surrounding pixels from the independent channel signal, $I[n]$, the spatial extent of this antagonism, or weighting of the extent was not addressed. Instead, Bagheri et al. [21] presented a centre-surround kernel M (Fig 4, 9 of [21]) that led to their ESTMD model having a band-pass region responsive to targets similar to the ones used in this work. Eq 10 is the same kernel as kernel M. The laterally inhibited independent ON and OFF channels were then clamped above zero to ensure the channel signals were non-negative. Similar to [16, 21], the local OFF channel outputs were delayed before correlating with undelayed local ON channel outputs to form a 'matched filter'. The OFF channels were delayed to enhance selectivity for dark targets. The matched filter formulation in the discrete-time domain is ($\tau = 25\,\text{ms}$, $T_s = 1\,\text{ms}$):

$$\text{ESTMD Output}[n] = ON[n] \cdot \text{D}(OFF[n]). \tag{11}$$

The OFF channel is temporally low-pass filtered – the delay operator, D was obtained using a temporal low-pass filter, similar to the one described in Eq 8. Mechanisms introduced here are our contributions to extending the ESTMD model to obtain a biologically plausible directionally selective small-field STMD model.

**S1 Video. Example preceding optic flow video.** Video at 60 fps of an example stimulus used in the preceding optic flow experiments. The preceding optic flow is contra-directional (rightward) while the concurrent optic flow is stationary. The target moves leftward. The black ellipse indicates the boundary of the particular TSDN's receptive field at 50% of the maximum response. Data from [11].

**S2 Video. Example dot density video.** Video at 60 fps of an example stimulus used in the dot density experiments. The starfield background has a dot density of 500 dots/$m^3$ and is moving contra-directional to the target (rightward). The target moves leftward. The black ellipse indicates the boundary of the particular TSDN's receptive field at 50% of the maximum response. Data from [11].

## Acknowledgments

SN and KN thank Biomedical Engineering at SAHLN and the Botanic Gardens of Adelaide for their ongoing support. AG is funded by the Leverhulme Trust, KN by the US Air Force Office of Scientific Research (AFOSR, FA9550-23-1-0473) and the Australian Research Council (ARC, DP210100740 and DP230100006), TN by the EPSRC (grant EP/S030964/1) and the EU (grant no. 945539), and JK was funded by the EPSRC (grants EP/V052241/1 and EP/S030964/1).

## References

1. Ogawa Y, Nicholas S, Thyselius M, Nowotny T, Knight JC, Nordstrom K. Neural responses to reconstructed target pursuits. bioRxiv. 2023; p. 2023–05.
2. Roth G. Visual behavior in salamanders. vol. 14. Springer Science & Business Media; 2012.
3. Förster D, Helmbrecht TO, Mearns DS, Jordan L, Mokayes N, Baier H. Retinotectal circuitry of larval zebrafish is adapted to detection and pursuit of prey. elife. 2020;9:e58596.
4. Lancer BH, Evans BJ, Fabian JM, O'Carroll DC, Wiederman SD. Preattentive facilitation of target trajectories in a dragonfly visual neuron. Communications biology. 2022;5(1):829.
5. Thyselius M, Ogawa Y, Leibbrandt R, Wardill TJ, Gonzalez-Bellido PT, Nordström K. Hoverfly (Eristalis tenax) pursuit of artificial targets. Journal of Experimental Biology. 2023;226(4):jeb244895.
6. Gonzalez-Bellido PT, Fabian ST, Nordström K. Target detection in insects: optical, neural and behavioral optimizations. Current opinion in neurobiology. 2016;41:122–128.
7. Nordström K, O'Carroll DC. Small object detection neurons in female hoverflies. Proceedings of the Royal Society B: Biological Sciences. 2006;273(1591):1211–1216.
8. Nordström K. Neural specializations for small target detection in insects. Current opinion in neurobiology. 2012;22(2):272–278.
9. Nicholas S, Leibbrandt R, Nordström K. Visual motion sensitivity in descending neurons in the hoverfly. Journal of Comparative Physiology A. 2020;206(2):149–163.

10. Nordström K, Barnett PD, O'Carroll DC. Insect detection of small targets moving in visual clutter. PLoS Biology. 2006;4(3):e54.

11. Nicholas S, Nordström K. Facilitation of neural responses to targets moving against optic flow. Proceedings of the National Academy of Sciences. 2021;118(38):e2024966118.

12. Reichardt W, Poggio T, Hausen K. Figure-ground discrimination by relative movement in the visual system of the fly: Part II: Towards the neural circuitry. Biological Cybernetics. 1983;46:1–30.

13. Hassenstein B, Reichardt W. Systemtheoretische analyse der zeit-, reihenfolgen-und vorzeichenauswertung bei der bewegungsperzeption des rüsselkäfers chlorophanus. Zeitschrift für Naturforschung B. 1956;11(9-10):513–524.

14. Borst A. Models of motion detection. Nature neuroscience. 2000;3(11):1168–1168.

15. Borst A, Haag J. Neural networks in the cockpit of the fly. Journal of Comparative Physiology A. 2002;188:419–437.

16. Wiederman SD, Shoemaker PA, O'Carroll DC. A model for the detection of moving targets in visual clutter inspired by insect physiology. PLoS ONE. 2008;3(7):e2784.

17. Wiederman SD, Shoemaker PA, O'Carroll DC. Correlation between OFF and ON channels underlies dark target selectivity in an insect visual system. Journal of Neuroscience. 2013;33(32):13225–13232.

18. Tanaka R, Clark DA. Object-displacement-sensitive visual neurons drive freezing in Drosophila. Current Biology. 2020;30(13):2532–2550.

19. Egelhaaf M. On the neuronal basis of figure-ground discrimination by relative motion in the visual system of the fly: II. Figure-detection cells, a new class of visual interneurones. Biological Cybernetics. 1985;52(3):195–209.

20. Barnett PD, Nordström K, O'carroll DC. Retinotopic organization of small-field-target-detecting neurons in the insect visual system. Current Biology. 2007;17(7):569–578.

21. Bagheri ZM, Wiederman SD, Cazzolato BS, Grainger S, O'Carroll DC. Performance of an insect-inspired target tracker in natural conditions. Bioinspiration & biomimetics. 2017;12(2):025006.

22. Longden KD, Krapp HG. Octopaminergic modulation of temporal frequency coding in an identified optic flow-processing interneuron. Frontiers in Systems Neuroscience. 2010;4:153.

23. Warzecha AK, Egelhaaf M. Response latency of a motion-sensitive neuron in the fly visual system: dependence on stimulus parameters and physiological conditions. Vision research. 2000;40(21):2973–2983.

24. Nicholas S, Supple J, Leibbrandt R, Gonzalez-Bellido PT, Nordström K. Integration of small-and wide-field visual features in target-selective descending neurons of both predatory and nonpredatory dipterans. Journal of Neuroscience. 2018;38(50):10725–10733.

25. Leibbrandt R, Nicholas S, Nordström K. The impulse response of optic flow-sensitive descending neurons to roll m-sequences. Journal of Experimental Biology. 2021;224(23):jeb242833.

26. Wiederman SD, O'Carroll DC. Discrimination of features in natural scenes by a dragonfly neuron. Journal of Neuroscience. 2011;31(19):7141–7144.

27. Gonzalez-Bellido PT, Peng H, Yang J, Georgopoulos AP, Olberg RM. Eight pairs of descending visual neurons in the dragonfly give wing motor centers accurate population vector of prey direction. Proceedings of the National Academy of Sciences. 2013;110(2):696–701.

28. Renart A, Machens CK. Variability in neural activity and behavior. Current opinion in neurobiology. 2014;25:211–220.

29. Hussaini MM, Evans BJ, O'Carroll DC, Wiederman SD. Temperature modulates the tuning properties of small target motion detector neurons in the dragonfly visual system. Current Biology. 2024;34(18):4332–4337.

30. Longden KD, Krapp HG. State-dependent performance of optic-flow processing interneurons. Journal of neurophysiology. 2009;102(6):3606–3618.

31. de Haan R, Lee YJ, Nordström K. Octopaminergic modulation of contrast sensitivity. Frontiers in Integrative Neuroscience. 2012;6:55.

32. Lin HT, Siwanowicz I, Leonardo A. Wireless recordings from dragonfly target detecting neurons during prey interception flight. bioRxiv. 2024; p. 2024–11.

33. Wellington W, Fitzpatrick SM. Territoriality in the drone fly, Eristalis tenax (Diptera: Syrphidae). The Canadian Entomologist. 1981;113(8):695–704.

34. Earland K, Lee M, Shaw P, Law J. Overlapping structures in sensory-motor mappings. PloS one. 2014;9(1):e84240.

35. Scott EK, Raabe T, Luo L. Structure of the vertical and horizontal system neurons of the lobula plate in Drosophila. Journal of Comparative Neurology. 2002;454(4):470–481.

36. Strother JA, Wu ST, Wong AM, Nern A, Rogers EM, Le JQ, et al. The emergence of directional selectivity in the visual motion pathway of Drosophila. Neuron. 2017;94(1):168–182.

37. Single S, Haag J, Borst A. Dendritic computation of direction selectivity and gain control in visual interneurons. Journal of Neuroscience. 1997;17(16):6023–6030.

38. Eichner H, Joesch M, Schnell B, Reiff DF, Borst A. Internal structure of the fly elementary motion detector. Neuron. 2011;70(6):1155–1164.

39. Jaxon-Mitchell, RJAoukar. HoverflyLab/FlyFly: Version 4.2.3; 2025. Available from: `https://doi.org/10.5281/zenodo.15044256`.

40. Brainard DH, Vision S. The psychophysics toolbox. Spatial vision. 1997;10(4):433–436.

41. Pelli DG. The VideoToolbox software for visual psychophysics: transforming numbers into movies. Spatial vision. 1997;10(4):437–442.

42. Srinivasan M, Guy R. Spectral properties of movement perception in the dronefly Eristalis. Journal of Comparative Physiology A. 1990;166:287–295.

43. Stavenga D. Angular and spectral sensitivity of fly photoreceptors. I. Integrated facet lens and rhabdomere optics. Journal of Comparative Physiology A. 2003;189:1–17.

44. Straw AD, Warrant EJ, O'Carroll DC. Abright zone'in male hoverfly (Eristalis tenax) eyes and associated faster motion detection and increased contrast sensitivity. Journal of Experimental Biology. 2006;209(21):4339–4354.

45. Halupka KJ, Wiederman SD, Cazzolato BS, O'Carroll DC. Discrete implementation of biologically inspired image processing for target detection. In: 2011 Seventh International Conference on Intelligent Sensors, Sensor Networks and Information Processing. IEEE; 2011. p. 143–148.

46. Jansonius N, Van Hateren J. Fast temporal adaptation of on-off units in the first optic chiasm of the blowfly. Journal of Comparative Physiology A. 1991;168:631–637.

47. Jansonius N, Van Hateren J. On-off units in the first optic chiasm of the blowfly II. Spatial properties. Journal of Comparative Physiology A. 1993;172:467–471.